Histidine orientation modulates the structure and dynamics of a *de novo* metalloenzyme active site

Matthew R. Ross[1,2], Aaron M. White[1], Fangting Yu[3], John T. King[4], Vincent L. Pecoraro, Kevin J. Kubarych[5]

Department of Chemistry, University of Michigan, Ann Arbor, MI 48109

[1]Equal contributions
[2]Present address: Department of Chemistry, University of Washington, Seattle, WA
[3]Present address: Department of Chemistry, Massachusetts Institute of Technology, Cambridge, MA
[4]Present address: Department of Materials Science and Engineering, University of Illinois, Urbana, IL
[5]To whom correspondence should be addressed. E-mail: kubarych@umich.edu.

Contents

1. Band position dynamics in a different peptide sequence

Another *de novo* metalloenzyme was studied using 2D-IR spectroscopy in addition to the **TRI**L2WL23H that was the focus of the main discussion. The apo-peptide of this additional peptide has the sequence **TRI**L2WK22QL23HK24Q, which is similar to the peptide considered in the main text, except the positively charged lysine residues on either side of the histidine site where the copper ion binds are replaced with neutral glutamine residues. This change reduces the charge on the tripeptide metal carbonyl system from +1 to -5, as two positive charges are neu-
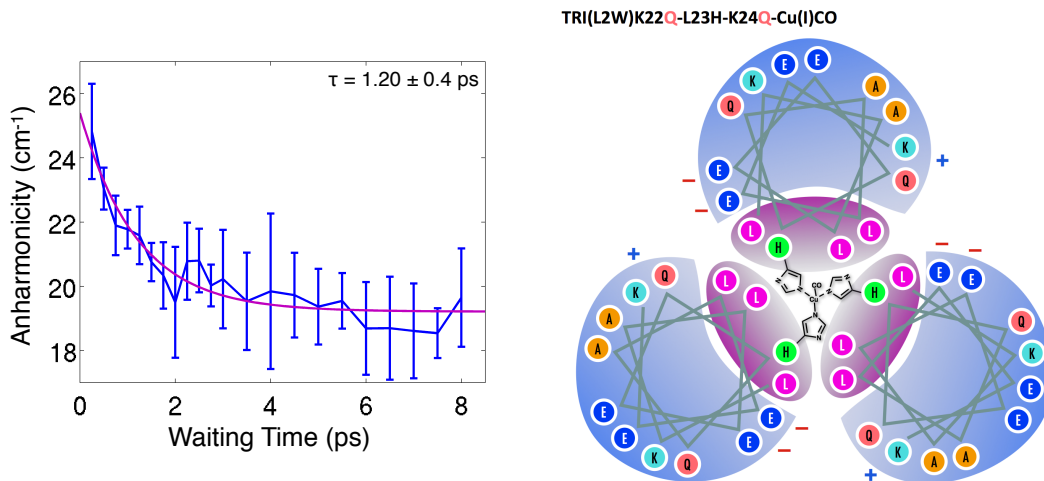

Figure S1: Apparent anharmonicity decay (*left*) of the mutant TRIL2WK22QL23HK24Q (*right*). While the decay rate and amplitude are different than observed for the peptide described in the main text, the band coalescence is clearly present in both cases. Differences may be due to the change in local electrostatics due to the preponderance of negative charges .

tralized in each of the three coils. This metalloenzyme also displays a time dependent merging of the two bands, as shown in Fig. S1. The decay is faster than in the **TRI**L2WL23H enzyme (1.20 ± 0.4 ps) and changes by a larger amount (6.18 ± 1.2 cm^{-1}), but the presence of nonequilibrium spectral dynamics in both peptides studied shows that it is not an exclusive feature of one mutation and implies that it is due to the more global structure of the peptide and not interaction with nearby charged residues. Moreover, given the attribution of the stretch-bend coupling to the histidine coordination, it would appear that modifying the charges on the external face of the peptide does not abolish the coupling. Rather, it may even be the case that the altered charge increases the coupling, resulting in a larger dynamical frequency shift.

2. Iron monocarbonyl complex shows no band merging dynamics

We wanted to discern if the band merging was a property of all transition metal monocarbonyls, as we had not studied any before and this signature has not been reported previously. A small molecule iron carbonyl, [$Fe^{II}(CO)(N4Py)$](ClO_4)$_2$, provided by Kodanko *et al.* [1] was studied as it has a single carbonyl on a metal center coordinated to multiple nitrogen atoms, similar to the TRI-family peptide. The molecule is also similar to the myoglobin and hemoglobin carbonyls previously studied by other groups [2,3], but has a higher CO stretching frequency, 2009 cm^{-1}, that is closer to the copper carbonyl presented in the main text than the iron-containing proteins. The anharmonicity of the iron carbonyl is similar to the copper carbonyl, 21 cm^{-1}, but does not show the same band coalescence seen in the metalloenzyme, as seen in Fig. S2*C-F*.

When comparing the 2D-IR spectra of the copper peptide and the iron carbonyl, one of the clearest differences is that the lineshape of the iron complex is much more homogeneously

broadened, which is attributed to the iron carbonyl being more solvent exposed than the copper carbonyl, which is in the hydrophobic interior of the coiled-coil structure. Although this homogeneous broadening lowers the resolution of the diagonal and off-diagonal peaks in the 2D-IR spectrum, it is still possible to determine the distance between the two bands, as shown in Fig.
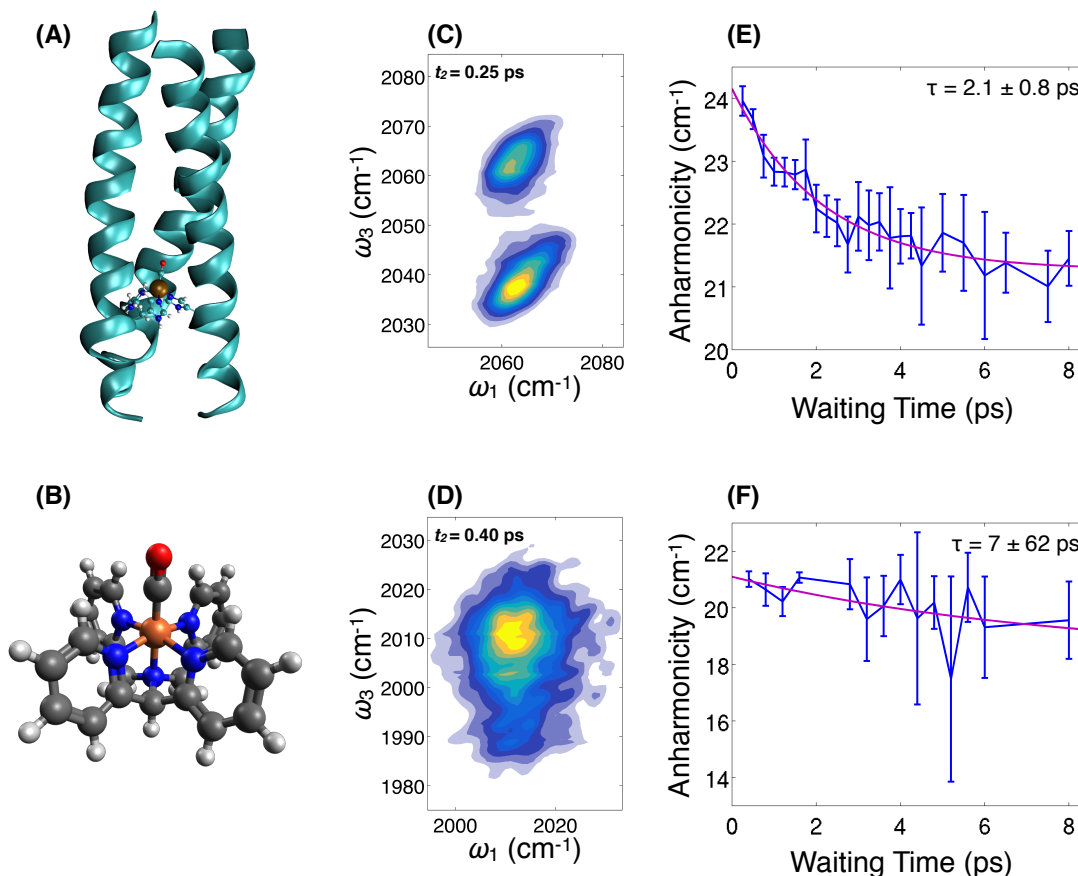

Figure S2: (*A*) Structure of the copper peptide Cu(I)(TRIL2WL23H)$_3$(CO)$^+$ discussed previously. (*B*) Structure of the Fe(II)(N4Py)(CO)$^{2+}$ small monocarbonyl used for comparison. (*C*) 2D-IR spectrum of the copper peptide at a waiting time of 0.25 ps. (*D*) 2D-IR spectrum of the iron complex at a waiting time of 0.40 ps. The carbonyl has a similar anharmonicity, but the peak is more homogeneously broadened, indicating more solvent interaction and making the anharmonicity more difficult to determine. (*E*) Apparent anharmonicity decay of the copper carbonyl, for reference. There is clearly a change in the splitting of the two bands. (*F*) Apparent change in anharmonicity of the iron carbonyl. The anharmonicity does not change by a measurable amount as shown by the uncertainty in the decay time of the offset exponential.

S2*F*. In this small iron complex the carbonyl bands do not appreciably merge, as shown by the poor fitting exponential with a decay time uncertainty that is an order of magnitude larger than the decay time.

We note here that recent work by Hunt *et al*. has found evidence for nonequilibrium frequency dynamics in the heme site of catalase using the NO bound ligand as a vibrational probe [4]. In those studies, they observed frequency modulations as a function of the time delay in a IR/IR pump probe transient absorption spectroscopy. In addition to the frequency modulations, they also reported dynamics of the apparent anharmonicity. The results were interpreted in terms of a coupling to a water-mediate intermolecular interaction via a low-frequency motion, similar to the present case (though we see no oscillations). The identity of the low-

frequency motion was not established, but presumably some approach similar to that taken here would be able to elucidate the detailed coupling and mechanism.

3. APBS and electric field calculations

The geometries used in the APBS calculations [5] were obtained from optimizing the geometry of the $(TRIL2WL23H)_3Cu(I)(CO)^+$ metalloenzyme using the same ONIOM scheme described earlier (B3LYP/6-311G(d,p):AMBER) with electronic embedding enabled. For each calculation, the Cu-C-O bond angle was frozen and the CO bond length was frozen at the ground (1.145 Å) or vibrationally excited length (1.260 Å) and the rest of the geometry was allowed to relax.

The electric field along the CO bond was analyzed using APBS by rotating the optimized coordinates to align the carbonyl with the z-axis. This produced a grid of electrostatic potential values and no interpolation was needed to determine electrostatic potential values along the carbonyl bond vector. Most of the charges used were the same as the default charges used in AMBER for standard amino acids [6]. The atoms included in the QM layer of the ONIOM calculation had charges assigned as generated by Gaussian according to the Merz-Singh-Kollman scheme for reproducing electrostatic potential [7-9]. Because the QM layer did not include the whole histidine residue, the total charge generated this way is not equal to 1.0, but is reasonably close, 1.64. Most of the radii were obtained using the PDB2PQR utility, but radii were not generated for the NH_2 groups, the metal carbonyl, or the hydrogen atoms in the methyl group of the acetyl caps [10,11]. The radii used are listed in Table S1.

Residue Name	Atom	Radius Å
NH$_2$	N	1.824
	H	0.600
Acetyl	H	0.600
Metal Carbonyl	Cu	2.000
	C	1.908
	O	1.661

Table S1: Atomic radii used for atoms not generated by PDB2PQR

These radii are the same as radii generated in other residues, with the exception of the copper atom, which was estimated to be 2 Å. This seems reasonable because the copper has a partial positive charge, so while it is larger than the second-period elements it will not be as large as an uncharged copper atom. Separate PQR files were generated for each optimized structure. There were 40 in total, one for each angle from 160 to 179 degrees, inclusive, in steps of one degree for both the ground and excited state. The geometry was centered on the carbon in the metal carbonyl and the CO bond was aligned with the z-axis as described above. Both the coarse and fine grids had dimensions of 50.0 by 45.0 by 75.0 Å to include the entire peptide in the grid. The output electrostatic potential was a grid of 97 by 97 by 1601 points to give a resolution of 0.52 Å in the X dimension, 0.46 Å in the Y dimension, and 0.05 Å in the Z dimension. The increased resolution was necessary along the Z dimension to monitor changes in the electrostatic potential and accurately calculate the electric field.

The electrostatic potential output by APBS is in units of k_BT/e_c where k_B is the Boltzmann constant, T is the temperature, and e_c is the charge on an electron. All calculations were run at the default temperature of 298.15 K, so the resulting electrostatic potential was converted to mV and is shown in Fig. S3*A*. The electrostatic potential is clearly dominated by the carbon and oxygen atoms of the carbonyl. The same calculations were performed with the charges on the CO set to zero to make a clearer electrostatic potential, shown in Fig. S3*B*. While indeed much

cleaner, there still was a large influence from the nearby copper atom that affected the electrostatic potential, so the copper charge was also set to zero for the remaining calculations. The electrostatic potential shown in Fig. S3*C* is thus the result of only the atoms in the apo-peptide and not the metal carbonyl. The ground and vibrationally excited states have similar but different electrostatic potentials and should reveal a difference in the electric field present at the carbonyl site.
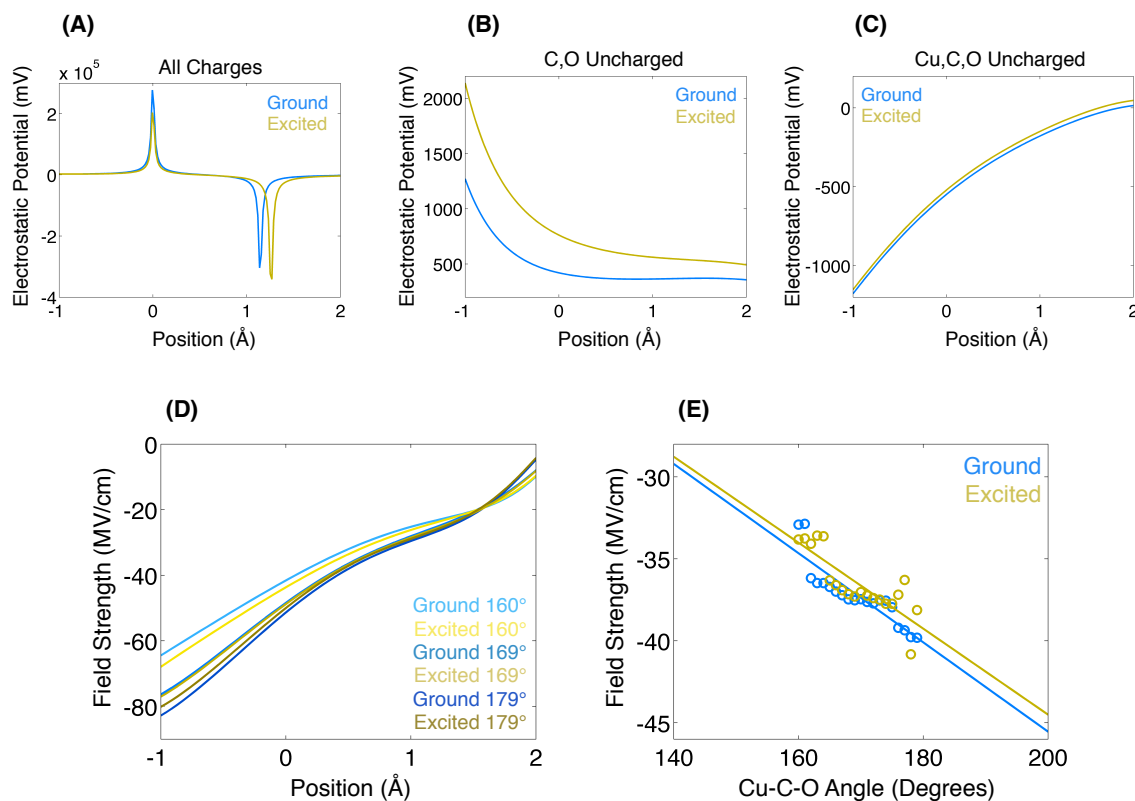

Figure S3: (*A*) Electrostatic potential along the CO bond vector, centered on the carbon atom for both ground and vibrationally excited CO bond lengths. The potential is dominated by the carbon and oxygen atom charges. (*B*) The same electrostatic potential, but with the CO charges set to 0. There is still a noticeable influence from the copper atom. (*C*) Electrostatic potential with the Cu, C, and O atoms' charges set to zero. (*D*) Electric field strength along the carbonyl bond vector derived from electrostatic potential for three different Cu-C-O bond angles. (*E*) Average field strength at the carbon and oxygen positions as a function of Cu-C-O bond angle for the ground and vibrationally excited states.

The electric field strength was calculated from the electrostatic potential along the CO bond vector for the ground and excited states. These field strengths are shown for three different Cu-C-O bond angles in Fig. S3*D*. While all six fields have a similar shape and intensity, the general trend is that the ground state fields are weaker and the larger angles have stronger field strength. Taking the average of the field strength at the carbon and oxygen atom positions in the carbonyl provided a method of comparing the field strength for each angle. These values, shown in Fig. S3*E*, are mostly between -35 and -40 MV/cm and increase roughly linearly with increasing Cu-C-O bond angle. From the linear fits there is a difference of 2.51 MV/cm between the ground state optimized geometry (171.5° Cu-C-O angle) and the excited state optimized geometry (164.8°).

4. Vibrational excitation alters the charge distribution on CO: Partial Charges (Mulliken) on the Cu, C and O Atoms

	Ground (no protein)	Excite (no protein)	Ground (with protein)	Excite (with protein)	Free CO [B3LYP/6-311G(d,p)] Ground	Free CO [B3LYP/6-311G(d,p)] Excite	Free CO [B3LYP/6-311++G(2d,2p)] Ground	Free CO [B3LYP/6-311++G(2d,2p)] Excite
$q(Cu)$, C	1.094350	1.119054	1.105311	1.129153	0.079896	0.13866	0.059075	0.136604
$q(C)$, C	-0.135865	-0.116676	-0.163153	-0.143809	-0.079896	-0.13866	-0.059705	-0.136604
$q(O)$, C	-0.124328	-0.195784	-0.193973	-0.273272	0.159792	0.27732	0.11878	0.273208
$q(C) - q(O)$, C	-0.011537	0.079108	0.03082	0.129463	1.127	1.227	1.125692	1.2375
d_{CO}, Å	1.13577	1.24934	1.14543	1.25999	0.18008	0.34027	0.13370	0.33809
dipole moment, D	-0.010157	0.06331	0.02690	0.10274	0.07989	0.13866	0.05907	0.13660

Table S2: Partial charges (Mulliken) on the Cu, C and O atoms of the copper site for the cases of no protein, with protein, and CO using two different bases. The lower level of theory is that used for the QM/MM calculations of the full peptide. The higher level of theory more faithfully captures the CO dipole moment in the ground state, whereas both return similar values for the extended geometry corresponding to the first vibrationally excited state.

5. Stark effect frequency shifts

The rather large electric field magnitude could provide a rationale for both the vibrational frequency shift and the coupling of the carbonyl stretching mode to the angle coordinate which drives the nonequilibrium dynamics. The argument is as follows: vibrational excitation alters the charge distribution on the CO (see partial charges above), causing it to realign in the field produced by the protein environment. In the new geometry, the projection of the field onto the CO bond changes, altering the frequency due to a Stark effect. In our model of the electric field, we find that the CO experiences a reduced electric field projection as the Cu-C-O angle deviates from 180°. In fact, the 6° geometrical change corresponds to a change in electric field magnitude of roughly -2 MV/cm, or 5% of the initial field magnitude. To estimate the frequency shift associated with the field change, we carried out vibrational Stark effect calculations by computing vibrational frequencies of optimized geometries of the smaller cluster [Cu(EtIm)$_3$CO] in the presence of finite fields. Using field values of -0.5, 0, and +0.5 MV/cm oriented parallel to the CuCO bond in the field-free geometry, we obtained a linear Stark tuning rate of 0.68 cm^{-1}/(MV/cm), which, when combined with the electric field change, yields a 1.4 cm^{-1} frequency shift [12]. The discrepancy of a factor of 2 in the magnitude of the frequency shift is likely to be within the range of uncertainty in our electrostatic potential calculation, but given the general agreement with other CO Stark tuning rates, it is unlikely that our DFT derived Stark tuning rate is incorrect by such a large magnitude. Instead of ascribing the majority of the frequency shift to
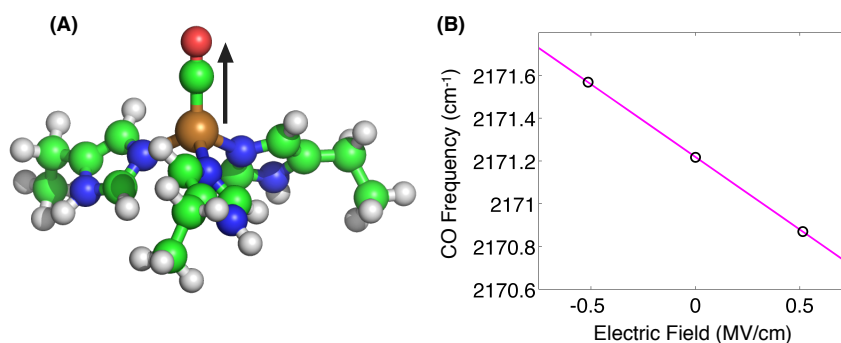

Figure S4: (*A*) Geometry of the Cu(EtIm)$_3$CO$^+$ system with an arrow pointing in the direction of a positive applied electric field, aligned with the Cu-C bond vector. (*B*) Unscaled CO stretching frequencies from DFT calculations for three different applied electric field values. The magenta line is a linear fit of the three points that gives a Stark tuning rate of 0.7 cm^{-1}/(MV/cm).

a typical vibrational Stark effect, we argue below that the primary origin of the shift is the geometrical change, which is itself driven by the long-range electrostatics.

5a. Calculation of Stark tuning rate

The Stark tuning rate of the carboxymetalloenzyme was estimated by performing geometry optimizations and frequency calculations on the small molecule analogue discussed previously with an applied electric field of varying strength using the Gaussian09 package. The dipole field was aligned with the Cu-C bond in the Cu(I)(EtIm)$_3$(CO)$^+$ system, pointing towards the oxygen atom in the carbonyl when the field was positive, as shown in Fig. S4*A*. Field strengths of +0.5 and -0.5 MV/cm were used and resulted in small shifts of the CO stretching frequency from the field-free frequency calculation, as shown in Fig. S4*B* [12]. A Stark tuning rate of 0.679 cm^{-1}/(MV/cm) was calculated by fitting the unscaled frequency change of these three points as a function of the electric field strength. This value should be reasonably close to the tuning rate of the actual peptide, and is accurate enough for the rough calculations we wanted to perform.
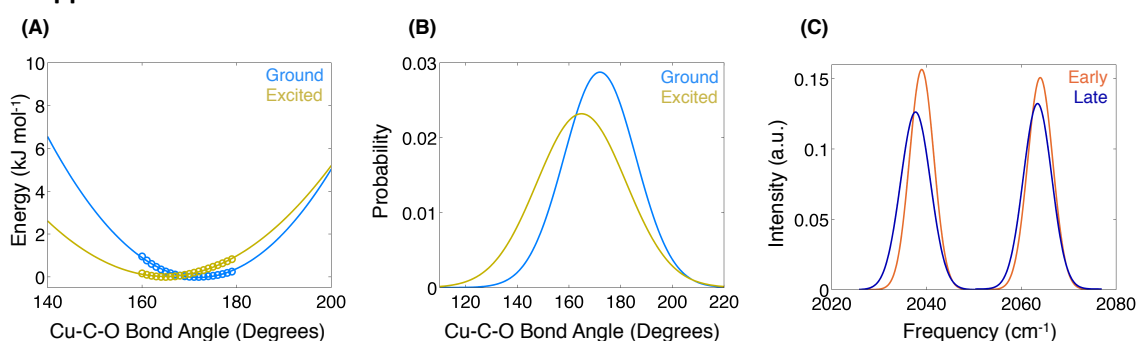
5b. Application to APBS results

Figure S5: (*A*) Potential energy of the Cu-C-O bond angle with ONIOM calculated energies shown as circles and quadratic fits shown as lines. The blue and yellow data refer to the ground and vibrationally excited states, respectively. (*B*) Boltzmann distributions at a temperature of 298 K for the ground and excited states. (*C*) In orange is the frequency distributions for the 0-1 and 1-2 transitions expected from the Stark tuning rate, the electric field strength as a function of Cu-C-O bond angle, and the bond angle distribution. In blue is the same frequency distribution after vibrational excitation and the angle distribution has had time to reach the excited distribution.

We wanted to obtain frequency distributions of the 0-1 and 1-2 transitions of the CO stretching mode to characterize how the Stark effect would influence the bands observed with 2D-IR spectroscopy when only accounting for the Stark tuning rate. This was done using Cu-C-O bond angle distributions, the electric field present from the peptide at each angle, and the Stark tuning rate calculated previously. Two different angle distributions (Fig. S5*B*) were generated for the ground and excited state potential energy of the Cu-C-O bond angle, shown in Fig. S5*A*, by assuming a Boltzmann distribution for the Cu-C-O angle potentials at a temperature of 298.15 K. These two distributions correspond to equilibrium distributions for the ground and vibrationally excited states of the peptide. The angle distributions were converted to electric field distributions using the field mapping discussed previously and shown in Fig. S3*E*. These field distributions were then translated into frequency distributions using the calculated Stark tuning rate of 0.68 cm^{-1}/(MV/cm). These frequency distributions were then centered around the 0-1 or 1-2 transition frequency to simulate the diagonal or off-diagonal peak present in the 2D-IR spectra.

To simplify the frequency distribution calculations, two different situations were considered. First, early waiting times were considered, where molecules that propagate through the waiting time in the excited state do not relax to an equilibrium angle distribution. In this case, both the ground and excited state would be expected to have the same angle distribution. Both

the 0-1 and 1-2 distributions are expected to have similar widths, as shown in Fig. S5*C* in the orange curve. The second situation is at later times, when the excited molecules have relaxed to an equilibrium angle distribution. This means that there are three total species to account for in the late time frequency distributions: molecules that spend the waiting time in the ground state and therefore will still have the ground state angle distribution and a center frequency of 2064 cm^{-1}. The other two frequency distributions are from molecules that propagate the waiting time in the excited state and are then either excited again, giving them a frequency near the normal 1-2 frequency, or undergo stimulated emission and have a frequency near the regular 0-1 frequency. Both of these later frequencies will be redshifted by a few wavenumbers, as the excited equilibrium angle distribution is centered on an angle that has a less negative field present, so the frequencies are expected to be slightly less, as shown in Fig. S4*B*. The end result of this is shown in Fig. S5*C* as the blue peaks. Both peaks are redshifted, but because only part of the 0-1 peak frequencies are expected to redshift the entire band does not shift as much as the 1-2 peak. From this we would expect the 0-1 band to redshift by 0.57 cm^{-1} and the 1-2 band to redshift by 1.3 cm^{-1}, assuming the shift was due only to the change in electric field because of the Cu-C-O bond angle decreasing after vibrational excitation. Because the 1-2 band actually blueshifts, we suspect there are additional factors affecting the CO frequency, such as the geometry distortion upon excitation.

5c. Comparison with heme proteins

From the work of Hochstrasser [13], we can correlate Fe-C-O bond angle with the CO stretching frequency. Since small model compounds do not exhibit such distorted bond angles, we rely upon the protein environment to provide the distortion driving force.

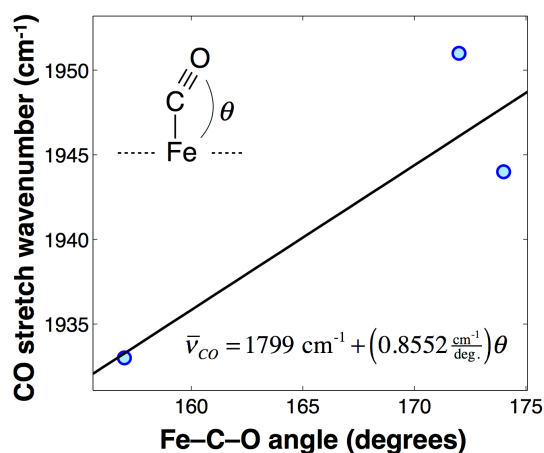| Species	MbCO	MbCO	HbCO
CO frequency (cm^{-1})	1933	1944	1951
FeCO angle (degrees)	157	174	172

Figure S6: Correlation between CO stretching frequency and the FeCO bond angle from Ref. 13. The fit allows a rough estimate of CO stretch for a given change in bond angle. In our case, we find a 6° bond tilt upon vibrational excitation, which would correspond to a 5 cm^{-1} frequency shift, which is similar to our 3-4 cm^{-1} observation.

6. Histidine distortion in ONIOM and DFT calculations

As seen in Fig. S7, most of the non-carbonyl atoms in the vibrationally labeled peptide are not displaced when the CO stretching mode is excited. The atoms in the small molecule analogue are more easily displaced because the rigid peptide backbone is not present, but the change in geometry is still fairly small, with an RMSD of 0.023 Å for the non-carbonyl atoms, compared to 0.015 and 0.008 Å for the same atoms in the ONIOM geometries with and without electronic embedding, respectively. There does not appear to be an obvious geometrical change associat-
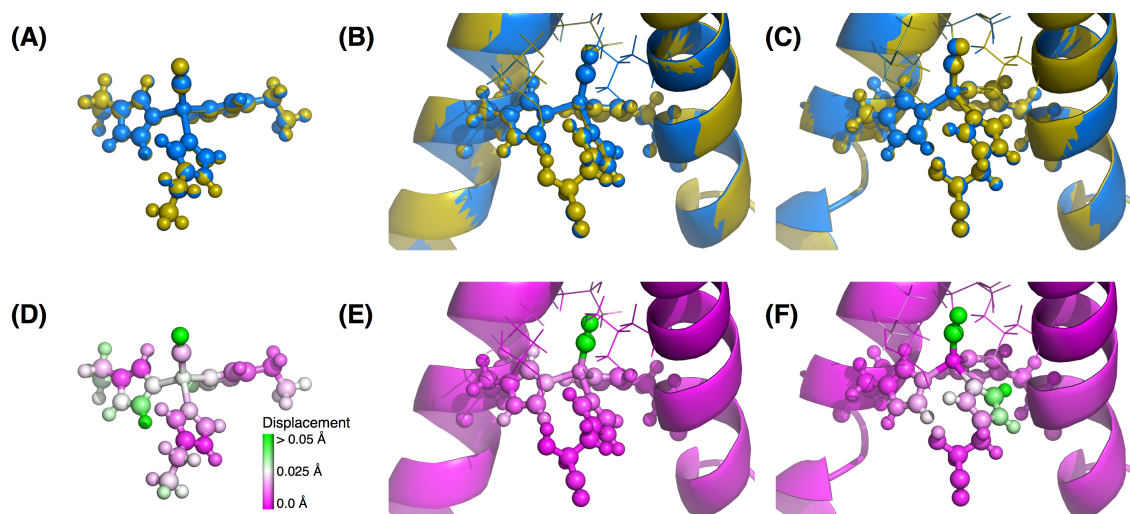

Figure S7. The optimized structures of the ground (blue) and vibrationally excited (yellow) states for the small molecule analogue (*A*), peptide calculated with ONIOM without electronic embedding (*B*), and peptide modeled with ONIOM including electronic embedding (*C*). The average of those two structures are shown (*D-F*) color coded to show the amount of displacement upon vibrational excitation with pink atoms remaining stationary and green atoms having the greatest displacement.

ed with the carbonyl tilting, such as a large change in the histidine-copper-carbonyl dihedral angle or the histidine-copper bond distance. The C_δ-N_ε-Cu-C dihedral angle does differ in each of the three cases pictured in Fig. S7 – the average dihedral angle is 48.6° for the small molecule, 60.6° for the peptide without electronic embedding, and 73.0° for the peptide with electronic embedding. The relationship between the dihedral angle and the Cu-C-O angle was explored by freezing the dihedral angle for each of the three ethylimidazole rings in the small molecule analogue and allowing the rest of the geometry to optimize. This was done for the ground state and the vibrationally excited state as described in the main text, resulting in the trend shown in Fig. S8.

For fixed dihedral angles near the optimized angle (average 48.6° from the three rings), there was little difference in the Cu-C-O angle when the geometry was optimized with the carbonyl 10% longer. However, the coupling between the Cu-C-O tilting and CO stretching modes was greater when the dihedral became more distorted. From this small molecule DFT calculation alone, we would expect an angle difference of ~1° upon excitation for the dihedral angles from the ONIOM geometry without electronic embedding, when the actual angle was found to change by 2.8°. Similarly, the expected change given the dihedral angles from the ONIOM geometry with electronic embedding is ~10°, while the calculated difference is 6.7°. The small difference from the expected angle change is a reasonable error, considering the frozen dihedral angle calculations were performed on only the small molecule analogue and the dihedral angles were not allowed to change upon vibrational excitation.
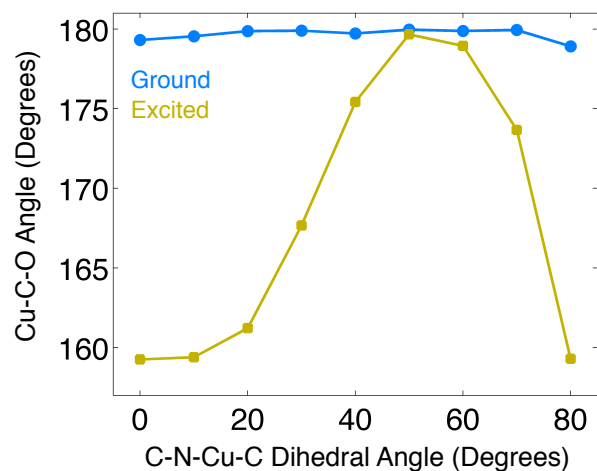
Figure S8: Calculated Cu-C-O bond angles when the C-N-Cu-C dihedral angles are frozen at a particular value for the (EtIm)$_3$CuCO small molecule analogue. The ground state shows little dependence on the dihedral angle, while the excited state changes considerably when the dihedral angle is sufficiently distorted.
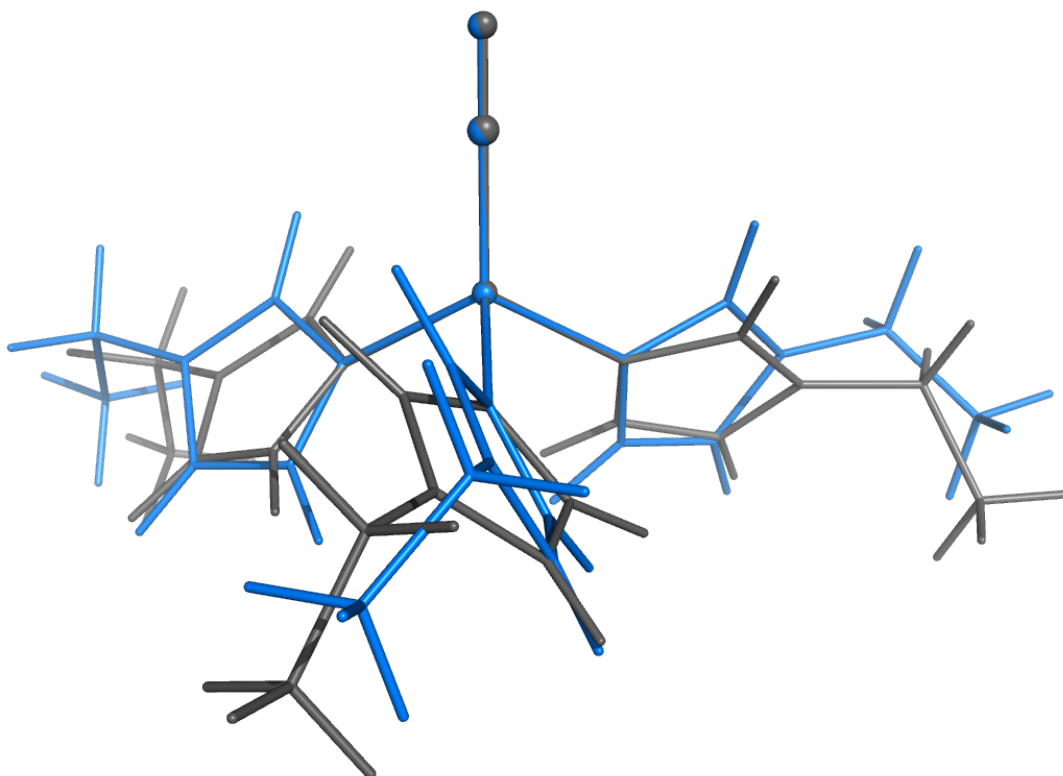

Figure S9: Geometries of DFT optimized (grey) and dihedral angle constrained at 20° (blue) for the CO vibrational ground state. Despite the large change in His coordination, the Cu-C-O bond angle is not altered.

7. Morse potential parameters

The Morse oscillator potential function is:

$$V(x) = D_e \left[\left(1 - e^{-a(x-x_e)} \right)^2 - 1 \right] \tag{S1}$$

where the two parameters are the dissociation energy, D_e, and the stiffness, a. The equilibrium position, x_e, is independently adjustable.

The solutions to the Morse oscillator eigenvalue problem are:

$$\psi_n(x) = z^{A\rho_n} \exp(-z) \, {}_1F_1\left(-n, 1 + 2A\rho_n, 2z\right) \tag{S2}$$

in which the following definitions are made:

1. $z = \dfrac{\sqrt{2D_e\mu}}{ah} \exp(-ax)$ $\qquad$ (S3)

where μ is the reduced mass and h is Planck's constant.

2. $A = \dfrac{\sqrt{2\mu}}{ah}$ $\qquad$ (S4)

3. $\rho_n = \sqrt{D_e} - \dfrac{n + \frac{1}{2}}{A}$ $\qquad$ (S5)

4. ${}_1F_1\left(-n, 1 + 2A\rho_n, 2z\right)$ is the confluent hypergeometric function of the first kind.

The energy eigenvalues are:

$$E_n = -D_e + hc\omega_e\left(n + \tfrac{1}{2}\right) - \frac{(hc\omega_e)^2}{4D_e}\left(n + \tfrac{1}{2}\right)^2 \tag{S6}$$

where $\omega_e = \dfrac{a}{2\pi c}\sqrt{\dfrac{2D_e}{\mu}}$.

The values of the constants that yield the observed fundamental frequency and initial anharmonicity are:

$m = 1.1386 \times 10^{-26}$ kg
$a = 2.21$ Å^{-1}
$D_e = 1.803 \times 10^{-18}$ J
$x_e = 1.10$ Å

With these parameters, the $n = 0$ to $n = 1$ transition is 2063.24 cm^{-1}, and the anharmonicity is 23.9986 cm^{-1}.

The expectation values of position are found to be:

$$\langle x \rangle = \int_{-\infty}^{\infty} \psi_n^*(x)(x - x_e)\psi_n(x)\,dx \qquad\qquad \text{(S7)}$$

$n = 0$: $\quad \langle x \rangle$ = 1.1476 Å

$n = 1$: $\quad \langle x \rangle$ = 1.24885 Å

$n = 2$: $\quad \langle x \rangle$ = 1.36014 Å

The change in bond length is therefore 1.24885 Å - 1.1476 Å = 0.10125 Å, which is roughly 10% of the $n = 0$ bond length.
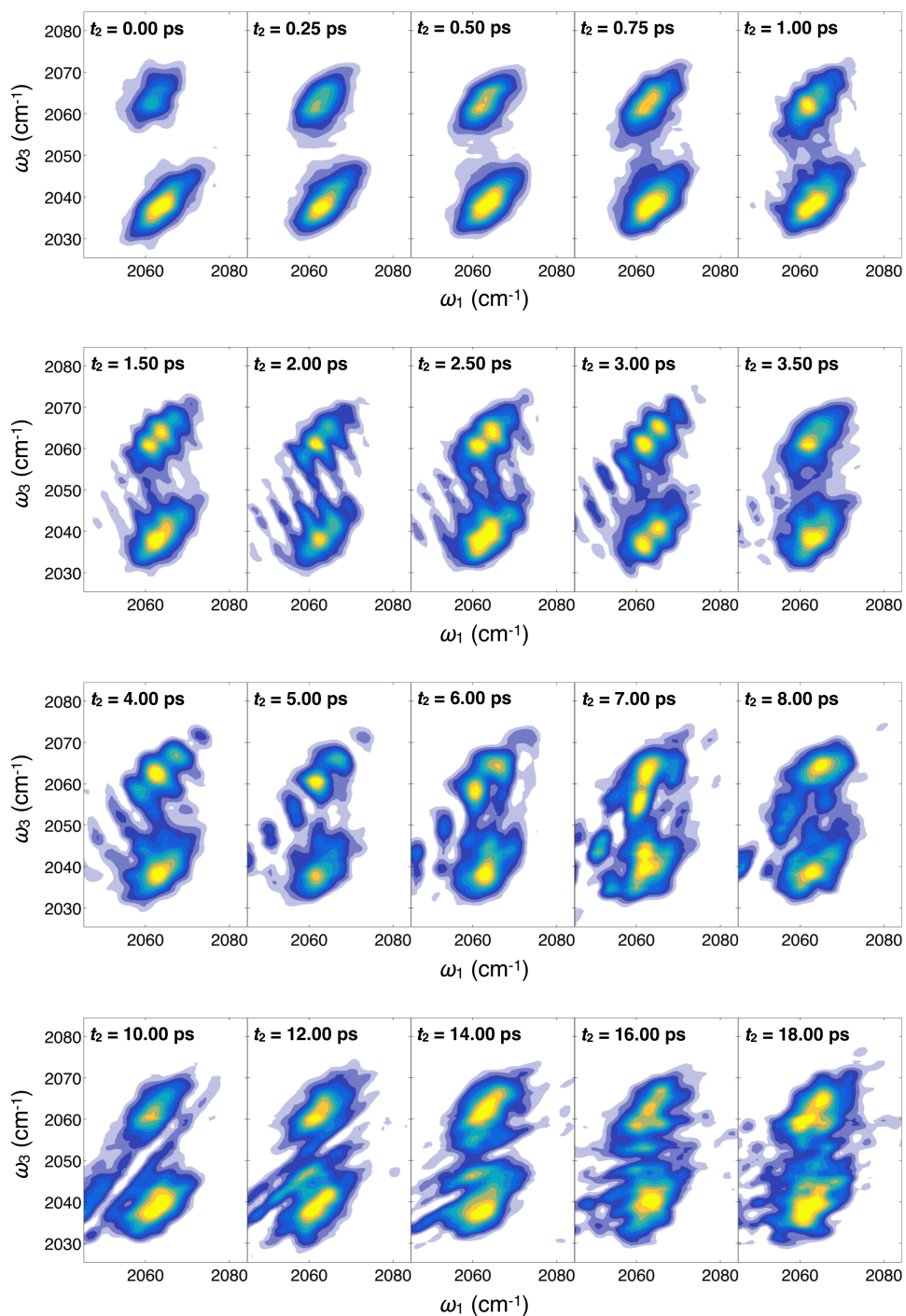
8. Additional 2D-IR spectra

Figure S10: Absolute magnitude 2D rephasing spectra of Cu(I)(**TRI**L2WL23H)$_3$(CO)$^+$ at various waiting times.

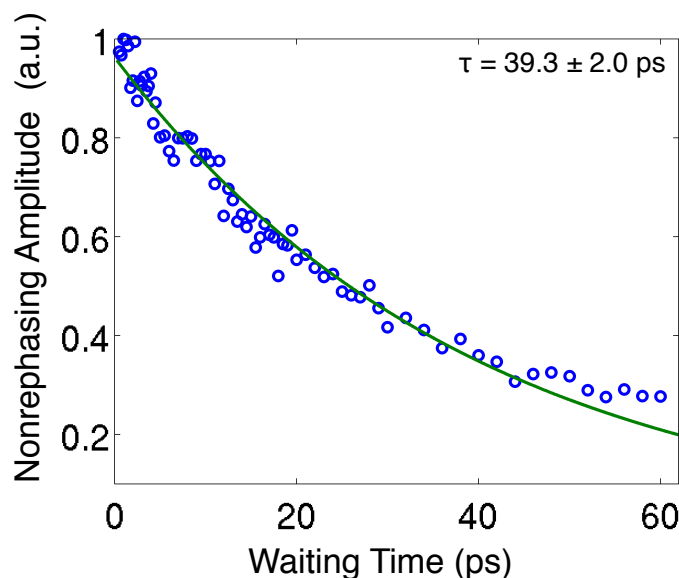## 9. Determination of vibrational lifetime

$\tau = 39.3 \pm 2.0$ ps

Figure S11: The vibrational lifetime of the carbonyl was determined to be 39 ps by finding the decay time of the excited state absorption band in the nonrephasing spectra.

10. Calculation of histidine dipole moment

Atom	TRI charge	CCO charge
CB	-0.4566	0.0971
HB1	0.0679	-0.0113
HB2	0.1253	-0.0113
CG	0.4615	0.1642
ND1	-0.5290	-0.1160
HD1	0.4383	0.0616
CE1	0.1454	-0.0109
HE1	0.2233	0.0088
NE2	-0.1904	0.1528
CD2	-0.4412	-0.2485
HD2	0.2642	0.1410
Cu	0.1546	-0.0741

Table S3: Average partial charges for atoms in histidine residues of Cu(I)(**TRI**L2WL23H)$_3$(CO)$^+$ (this work) and cytochrome c oxidase Cu$_B$ (Ref. 14)

The average atomic charges from the ONIOM calculations using the Merz-Singh-Kollman scheme for reproducing electrostatic potential [8,9] are found to be comparable to the RESP charges obtained for the Cu$_B$ site in cytochrome c oxidase [14], shown in Table S3. There is a greater charge separation, and thus a larger dipole moment, between the C$_\varepsilon$-H, C$_\delta$-H, and N$_\delta$-H pairs, which could produce increased hydrogen bonding to the carbonyl or nearby side chains. Using the charges above, plus the calculated atomic charge of 0.1827 e on the alpha-carbon, the dipole moment of each histidine residue was calculated from the center of the imidazole ring, as shown in Fig. S12. This average dipole moment of 3.6 D is large enough to induce a torque when exposed to the electric field of the peptide, distorting the C$_\delta$-N$_\varepsilon$-Cu-C dihedral angle.

11. References

(1) Jackson, C. S.; Schmitt, S.; Dou, Q. P.; Kodanko, J. J. *Inorg. Chem.* **2011**, *50*, 5336-5338.

(2) Bagchi, S.; Nebgen, B. T.; Loring, R. F.; Fayer, M. D. *J. Am. Chem. Soc.* **2010**, *132*, 18367-18376.

(3) Ventalon, C.; Fraser, J.; Vos, M.; Alexandrou, A.; Martin, J.; Joffre, M. *Proc. Natl. Acad. Sci. U. S. A.* **2004**, *101*, 13216-13220.

(4) Adamczyk, K.; Simpson, N.; Greetham, G. M.; Gumiero, A.; Walsh, M. A.; Towrie, M.; Parker, A. W.; Hunt, N. T. *Chem. Sci.* **2015**, *6*, 505-516.

(5) Baker, N. A.; Sept, D.; Joseph, S.; Holst, M. J.; McCammon, J. A. *Proc. Natl. Acad. Sci. U. S. A.* **2001**, *98*, 10037-10041.

(6) Cornell, W. D.; Cieplak, P.; Bayly, C. I.; Gould, I. R.; Merz, K. M.; Ferguson, D. M.; Spellmeyer, D. C.; Fox, T.; Caldwell, J. W.; Kollman, P. A. *J. Am. Chem. Soc.* **1995**, *117*, 5179-5197.

(7) Frisch, M. J.; Trucks, G. W.; Schlegel, H. B.; Scuseria, G. E.; Robb, M. A.; Cheeseman, J. R.; Scalmani, G.; Barone, V.; Mennucci, B.; Petersson, G. A.; Nakatsuji, H.; Caricato, M.; Li, X.; Hratchian, H. P.; Izmaylov, A. F.; Bloino, J.; Zheng, G.; Sonnenberg, J. L.; Hada, M.; Ehara, M.; Toyota, K.; Fukuda, R.; Hasegawa, J.; Ishida, M.; Nakajima, T.; Honda, Y.; Kitao, O.; Nakai, H.; Vreven, T.; Montgomery Jr., J. A.; Peralta, J. E.; Ogliaro, F.; Bearpark, M. J.; Heyd, J.; Brothers, E. N.; Kudin, K. N.; Staroverov, V. N.; Kobayashi, R.; Normand, J.; Raghavachari, K.; Rendell, A. P.; Burant, J. C.; Iyengar, S. S.; Tomasi, J.; Cossi, M.; Rega, N.; Millam, N. J.; Klene, M.; Knox, J. E.; Cross, J. B.; Bakken, V.; Adamo, C.; Jaramillo, J.; Gomperts, R.; Stratmann, R. E.; Yazyev, O.; Austin, A. J.; Cammi, R.; Pomelli, C.; Ochterski, J. W.; Martin, R. L.; Morokuma, K.; Zakrzewski, V. G.; Voth, G. A.; Salvador, P.; Dannenberg, J. J.; Dapprich, S.; Daniels, A. D.; Farkas, Ö.; Foresman, J. B.; Ortiz, J. V.; Cioslowski, J.; Fox, D. J.; Gaussian, Inc.: Wallingford, CT, USA, 2009.

(8) Besler, B. H.; Merz, K. M.; Kollman, P. A. *J. Comput. Chem.* **1990**, *11*, 431-439.

(9) Singh, U. C.; Kollman, P. A. *J. Comput. Chem.* **1984**, *5*, 129-145.

(10) Dolinsky, T. J.; Czodrowski, P.; Li, H.; Nielsen, J. E.; Jensen, J. H.; Klebe, G.; Baker, N. A. *Nucleic Acids Res.* **2007**, *35*, W522-W525.

(11) Dolinsky, T. J.; Nielsen, J. E.; McCammon, J. A.; Baker, N. A. *Nucleic Acids Res.* **2004**, *32*, W665-W667.

(12) Franzen, S. *J. Am. Chem. Soc.* **2002**, *124*, 13271-13281.

(13) Moore, J. N.; Hansen, P. A.; Hochstrasser, R. M. *Proc. Natl. Acad. Sci. U. S. A.* **1988**, *85*, 5062-5066.

(14) Tipmanee, V.; Blumberger, J. *J. Phys. Chem. B* **2012**, *116*, 1876-1883.